International Journal of Heat and Mass Transfer 261 (2026) 128606

Contents lists available at ScienceDirect

International Journal of Heat and Mass Transfer

journal homepage: www.elsevier.com/locate/hmt

# Diffusive-reactive mass transfer in oncology: Foundations and metrics of realistic therapy simulations

Gianpaolo Ruocco

*Department of Engineering, University of Basilicata, Via dell'Ateneo Lucano, 85100 Potenza, Italy*

ARTICLE INFO

*Keywords:*
Mass transfer
Tumor growth
Proliferation
Computational prognosis modeling

ABSTRACT

In the framework of oncology care, therapeutic outcomes can be explored through computational modeling. The proliferation of solid tumors and the action of anticancer therapies arise from the interplay between local growth kinetics, the diffusion of tumor cells within surrounding tissues, and the transport, effectiveness, and metabolism of administered drugs. In this study, we formalize the constitutive assumptions that allow these mechanisms to be represented within a common CFD platform.

Computational modeling can accelerate oncological research by predicting patient-specific treatment responses with enhanced precision, ensuring that simulations remain consistent with biological and clinical constraints. As the adoption of quantitative metrics is essential to support emerging digital-health paradigms, we introduce a modified mass Damköhler number Da as a descriptor of therapeutic efficacy. By formulating this metric across a combination of therapeutic branches, we establish a framework that predicts how treatment performance may improve through controlled modifications of dosage while conserving total drug exposure.

Dosages that are even slightly incremented (10%) in correspondence of strong negative Da transients (from about $1 \cdot 10^6$ on, in a study case) allowed in a case of study for improvement of residual lesion volume reduction by a fraction of $cm^3$, while accelerating complete healing by some 15 days in another. This study provides a set of engineering-oriented tools for characterizing and forecasting tumor dynamics and treatment response, offering a structured approach for analyzing the competition between proliferation and drug challenge in solid-tumor therapy.

## 1. Introduction

Breast cancer (BC) ranks as the most common cancer among women and remains a major contributor to cancer-related deaths [1]. Computational modeling considering tumor mass dynamics and its interaction with therapeutic drug can be cast for each patient, so that valuable insights can be gained, potentially leading to improved treatment strategies and patient outcomes. Such virtual twinning can be brought forth by using 3D solvers capable of handling nonlinear, multiscale phenomena such as tumor growth and therapeutic response, which involve coupled effects of mass transfer, cellular biomechanics, and biochemical metabolism. These tools can be also envisaged in the framework of BC, where neoadjuvant therapy (NAT) is commonly delivered, referring to the clinical goals of prompting tumor shrinkage, improving operability, and enabling breast conserving surgery.

The available contribution from engineering computation in this field of application is extensive and rapidly evolving; thus, the analysis of the foundation framework can only partially capture the breadth and relevance of existing relevant research. Gatenby and Gawlinski's reaction–diffusion model provided a pioneering quantitative framework to describe and predict cancer invasion dynamics, serving as a foundation for subsequent computational approaches in solid tumor prognosis and therapy optimization [2]. Anderson et al. provided a seminal mathematical framework for tumor invasion and metastasis, highlighting the critical role of computational models in elucidating cancer dynamics and informing clinical strategies for disease progression and management [3]. Stamatakos et al. introduced the Oncosimulator, a pioneering multilevel simulation system enabling clinically relevant modeling of tumor growth and therapeutic responses, emphasizing on the computational tools into oncology practice [4]. Cristini and Lowengrub presented yet another seminal approach to multiscale cancer modeling, combining experimental and mathematical perspectives to address tumor complexity, growth, and response, thereby advancing predictive modeling [5]. Specifically for BC, Weis et al. presented a mechanically coupled reaction–diffusion model capable of predicting breast tumor response to neoadjuvant chemotherapy, demonstrating the utility of integrated biophysical modeling for prognostic assessment

*E-mail address:* gianpaolo.ruocco@unibas.it.

https://doi.org/10.1016/j.ijheatmasstransfer.2026.128606
Received 17 November 2025; Received in revised form 28 January 2026; Accepted 24 February 2026
Available online 28 February 2026

and therapeutic planning in clinical oncology [6]. Ghaffari Laleh et al. reviewed classical mathematical models for tumor response to therapy, comparing predictive accuracy and data fitting for the two kinds of NATs (chemo- and immunotherapy) [7]. Yankeelov and co-workers' line of research the evolved into studies that employ increasingly more complex modeling approaches [8]. In contrast, a simplified tissue-scale approach to study NAT optimization conditions was more recently proposed by Ruocco and co-workers [9–13] that retains modeling simplicity while still offering strong validation potentials, while

Engineering metrics can play in favor of the adoption of computational modeling, offering quantifiable parameters to assess and optimize model performance. Dimensionless numbers that quantify the interplay between reaction rates and mass transfer in tumors, or indicators of diffusion and cell proliferation rates, could provide a physically consistent basis for model validation and comparison [14]. By incorporating such metrics, *in silico* models can be calibrated to reflect clinical variability, enhancing their predictive accuracy and resilience. Moreover, these metrics offer valuable insights into optimizing therapeutic interventions: drug diffusion efficiency or tumor response rates can be captured quantitatively to guide dosage adjustments or delivery methods. Thus, integrating engineering-based dimensionless analysis into oncological models not only improves alignment with clinical data but also supports the design of more personalized and adaptable therapeutic strategies.

In the present paper, a Damköhler-type metric linking reaction kinetics to diffusive transport is proposed for the first time to enable structured comparisons between simulated and clinical behaviors in BC proliferation and therapy; building on a realistic tissue-scale modeling framework, the proposed approach emphasizes model simplicity to enhance calibration robustness, interpretability, and translational applicability.

## 2. Analysis

Macroscopic histopathology of solid tumors, as for example in early-stage BC treated with NAT, can be seen as a transient diffusive-reactive mass transfer process in a stationary multiphase continuum, therefore dealing with the two transport effects intertwined with proper nonlinear source/sink terms, applied to the net transfer of different species such as cancer cells and drugs in biological/biochemical disequilibrium in a Region of Interest (ROI). In this modeling interpretation, regarding drug delivery, the effects of multiple mediating compartments and convection driven by interstitial fluid flow are neglected, as their impact is expected to be similar across patients and minimal over the weeks-long clinical timescale [15,16]. Additionally, extracellular matrix interactions or the influence of cancer-associated fibroblasts are not explicitly represented: their contributions are spatially much finer than the macroscopic length scale of the clinical ROI, then the detailed microstructure can be replaced by an effective tumor diffusion coefficient [17–19].

### 2.1. A macroscopic interpretation of tumor proliferation and cure

To perform a quantitative prognosis of oncological therapy, macroscopic tumor progress can be simulated to represent an integral metric or metabolic tumor volume descriptor $V(t)$ as in Fig. 1.**a**. This approach is common in multiscale oncology modeling, where continuous density fields are mapped to clinically observable quantities through integral or averaged descriptors [20]. Tumoral mass transfer modeling can be trained towards validation, starting from diagnostic imaging assessments of retrospective patients such as the one shown in Fig. 1.**b**, with the final aim to apply such prognostic computation to prospective (i.e. future) patients.

We define $t = 0$ as the time of diagnosis and the initiation of therapeutic regimen. Prior to that, during *free proliferation* (Phase I), the tumor lesion was originated from an initial occurrence at some time $t_\mathrm{i}$ in the past. After $t = 0$, therapy administration commences (Phase II), where the tumor undergoes *challenged proliferation*. Contemporary NATs for BC are administered with a sequence of therapeutic branches, but in Fig. 1.a, one branch is purported, only, for sake of simplicity, with the time-average $V$ decrement denoted by a red curve. Therapeutic regimens consist of a series of administrations; in each installment, nonlinear interactions are at play: between tumor growth rate with therapy (or pharmacodynamics, along the green curve marked by ), and with drug clearance onset (or pharmacokinetics, along the purple curve marked by ). Spanning a duration $\Delta t_\mathrm{s}$, the successful therapy leads to tumor regression; after this period, surgery is commonly performed if pathological Complete Response (pCR) is still unachieved (i.e. a finite residual tumor volume $\Delta V_\mathrm{s}$ is assessed). In fact, with $\Delta V_\mathrm{s}$ above a minimal threshold, a pathological relapse can be supported and *uncontrolled proliferation* will occur (Phase III).

For the aims of this study, the analysis refers to Phase I + Phase II sequence, only, with Phase II being the focus of quantitative prognosis.

### 2.2. Formulation of tumor proliferation

Computational oncology in continua can be based on a species concentration-based formulation. Solid tumor is seen as a single-phase tissue featuring a *cancer cells population*, that grows and invades a given ROI [3,5], during the sequence of Phases. When $\phi_\mathrm{c}$ represents the cancer cell density, or dimensionless cell volume in the biological matrix, Gompertzian logistics can be employed to describe the evolution (change rate) of cell density:

$$\frac{\mathrm{d}\phi_\mathrm{c}}{\mathrm{d}t} = -r\phi_\mathrm{c}\left(\mathbf{x}\right)\ln\left[\frac{\phi_\mathrm{c}\left(\mathbf{x}\right)}{K}\right] \tag{1}$$

where $1/r$ is a timescale constant and $K$ is the nominal carrying capacity of the ROI. Therefore, starting at the beginning of Phase I and continuing throughout the process up to Phase II completion, a governing diffusive-reactive PDE for transport of tumor mass can be applied in space $\mathbf{x}$ and time $t$, in terms of $\phi_\mathrm{c}$ [21]:

$$\frac{\partial\phi_\mathrm{c}}{\partial t} = \nabla\cdot\left[\mathbf{D}_\mathrm{c}\left(\mathbf{x},t\right)\nabla\phi_\mathrm{c}\left(\mathbf{x}\right)\right] + R_\mathrm{c} \tag{2}$$

### 2.3. Virtual biomarkers definition

During Phase II a series of one or more *drug species* is administered. Subsequently, starting at the beginning of Phase II (i.e. at $t = 0$, in the convention of Fig. 1.**a**) another set of governing diffusive-reactive PDEs for transport of each $j$th drug species can be applied to the ROI in terms of species concentrations $\phi_\mathrm{dj}$:

$$\frac{\partial\phi_\mathrm{dj}}{\partial t} = \nabla\cdot\left[\mathbf{D}_\mathrm{dj}\left(\mathbf{x},t\right)\nabla\phi_\mathrm{dj}\left(\mathbf{x}\right)\right] + R_\mathrm{dj} \tag{3}$$

In the following, the dependence of $\phi$s on space and time will be implied, for sake of simplicity.

In Eqs. (2), (3), source terms $R_\mathrm{i}$ can be respectively specified as

$$R_\mathrm{c} = -r\phi_\mathrm{c}\ln\left(\frac{\phi_\mathrm{c}}{K}\right) - \epsilon_\mathrm{PDj}\phi_\mathrm{dj} \tag{4}$$

and

$$R_\mathrm{dj} = \mathbf{d}_\mathrm{j}\left(t\right)\dot{m}_\mathrm{j} - \epsilon_\mathrm{PKj}\phi_\mathrm{dj} \tag{5}$$

having implied the dependencies of dependent variables with space and time.

When seeking model validation, the model formed by Eqs. (2)–(5) requires proper values for several embedded parameters or *virtual biomarkers*, that depend in turn upon a number of common clinical biomarkers, that are measurable indicators derived from patient data and imaging assessments. When dependent variables $\phi_\mathrm{c}$ and $\phi_\mathrm{dj}$ are denoted as molar concentrations, the following definitions and evaluations apply:

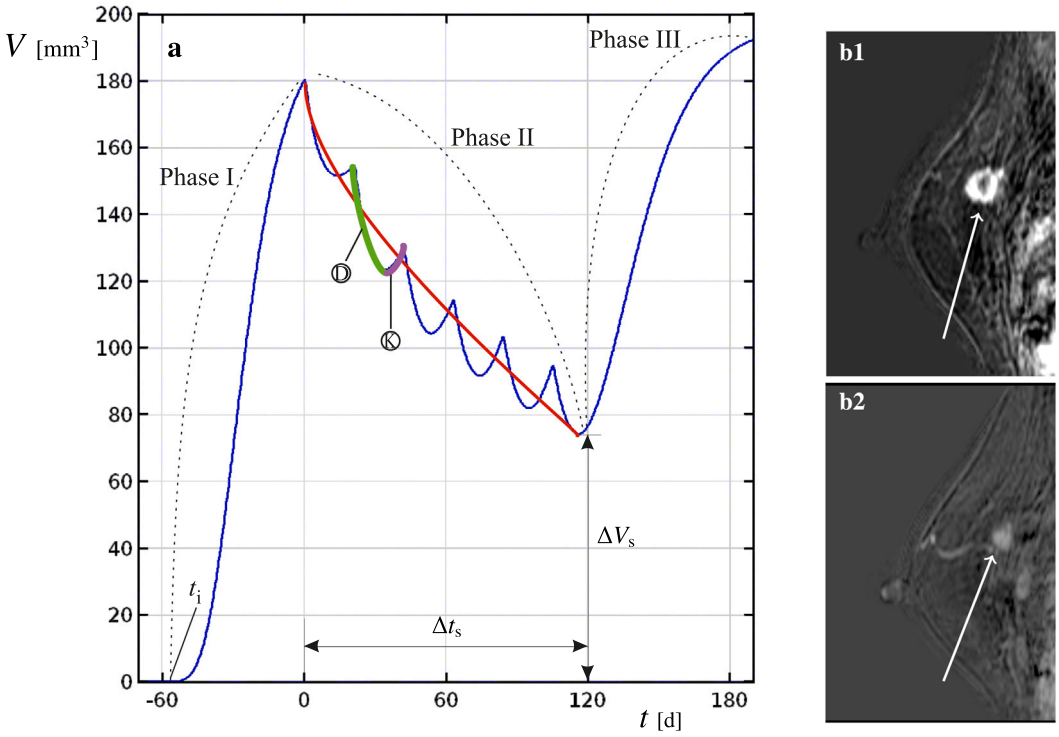


**Fig. 1.** (**a**) a sequence of *free*, *challenged* and *uncontrolled* tumoral proliferation encompassing Phases I to III, delineating metric or metabolic tumor volume progress $V$ versus time $t$ (blue line). A therapy is administered in Phase II, with the average $V$ progress denoted by a red line. During any installment of therapeutic cycle, the effect of the interaction between tumor growth rate and therapeutic dynamics can be marked by a green segment marked by , while the effect of the interaction between growth rate and drug clearance can be marked by a purple segment marked by . Tumor starting time $t_i$, therapeutic duration $\Delta t_s$ and residual tumor volume $\Delta V_s$ before possible surgical intervention are also indicated. (**b**) sagittal projections from Magnetic Resonance Imaging (MRI) assessment of sample BC patient [12], with indication of areas corresponding to tumoral lesions: (**b1**) right before Phase II ($t = 0$); (**b2**) right after Phase II ($t = \Delta t_s$). (For interpretation of the references to color in this figure legend, the reader is referred to the web version of this article.)

- $\mathbf{D}_c$ and $\mathbf{D}_{dj}$ are the effective binary diffusion coefficients for species $\phi_c$ and $\phi_{dj}$, respectively, in tensorial form to account for inherent variability (anisotropy/dishomogeneity/changes in time). In particular, $\mathbf{D}_c$ takes into account local tissue mechanics properties and related mechanical equilibrium. In uniform and constant-property biological matrix, $\mathbf{D} \equiv D$; typical values for $D_c$ are in the $10^{-12} - 10^{-13}$ m$^2$/s range [22], while $D_{dj}$ are in the $10^{-9} - 10^{-8}$ m$^2$/s range [23];
- $r$, the driving parameter for tumor proliferation, is the biological tumor conversion rate to account for creation of $\phi_c$. For a given patient cohort, $r$ is scaled nominally by a constant $r_0$ (assumed uniform across the cohort) reflecting the classification of BC at hand, such as invasiveness/aggressiveness/malignancy (i.e. a combination of histopathological type, grade and stage of the tumor). $r_0$ is taken as $1 \cdot 10^{-7}$ 1/s, while the personalized $r$ values are found depending on some clinical biomarkers extracted by the available retrospective data;
- $\epsilon_{PDj}$, the driving parameter for therapeutic action, is the nominal treatment efficiency, or aggregated pharmacodynamics behavior of the drug combination administered at the $j$th therapy branch. $\epsilon_{PDj}$ values are found in the $10^{-6}$–$10^{-4}$ 1/s range, again depending on some personalized clinical biomarkers;
- $\epsilon_{PKj}$ is the known effects of the plasma clearance, or pharmacokinetics behavior of the drug combination administered at the $j$th therapeutic branch, generally depending on each patient's weight and body surface area. With clearances commonly given in the $10^0 - 10^1$ l/h range, typical values of $\epsilon_{PKj}$ are found in the $10^{-6} - 10^{-4}$ 1/s range;
- for the administered drug, $\mathbf{d}_j$ is the normalized dose fraction of the therapeutic sequence, and $\dot{m}_j$ are the molar concentration rates (administered orally or by infusion, as proper), based on patient's mass, usually in the $10^{-4} - 10^{-2}$ mol/m$^3$s range.

### 2.4. Virtual biomarkers assessment towards model validation

To validate the model for each patient belonging to a retrospective cohort (same BC subtype and therapeutic sequence), whose driving clinical biomarkers and diagnostic imaging assessments are available, proper model training must be exercised, as alluded to earlier, to achieve the desired minimal deviations between $V^*$ and $V$ at the clinically available times, i.e. Phase II beginning and end ($t = 0$ and $t = \Delta t_s$, respectively).

To this end, the resulting best $(r, \epsilon_{PD_j})$ biomarker value set must be found to be applied uniformly over the cohort. Generally in BC, driving clinical biomarkers are taken as the levels of some receptor proteins (i.e. estrogen, progestin and human epidermal growth factor), antigen Ki-67, Tumor-Infiltrating Lymphocytes (TILs) and gut microbiota composition, before therapy begins. In this research, the tumor conversion rate is found as $r = \text{Ki67} \cdot r_0$, with the Ki-67 level representing the fraction of cells actively dividing within the tumor, therefore reflecting the aggressive behavior or malignancy. The nominal treatment efficiency $\epsilon_{PD}$ for common chemotherapies likewise depends on personalized Ki67 level, representing at the same time the likelihood of response; in some BC subtype, the TILs level reflects the extent of the host immune response against the tumor and may influence the outcome [11]. In case of combined immunotherapies, $\epsilon_{PD}$ is given by a personalized gut microbiota diversity index (DI) reflecting the microbiota classification [13], here scaled nominally by a constant $\epsilon_{PD0}$ (also assumed uniform across the cohort).

Finally, a third virtual biomarker $t_i$ value is assumed, for each patient, by precisely superimposing $V^*$ and $V$ for $t = 0$. While there

could be no clinical verification of the $t_i$ value assumption, as the tumor initiation event is unknown to both patient and diagnosing physician, the optimal $t_i$ can be iterated by knowing that a dimensionless free proliferation number FP range exists for any given cohort [10]:

$$\mathrm{FP} = |t_i| \cdot r \tag{6}$$

For the cohort at stake in this work, FPs lie between 1 and 2.

Following model validation, the resulting virtual biomarker value set allows for collection of relevant insights at the prospective level, ultimately providing a robust foundation for BC prognosis.

### 2.5. Lesion volume, initial, termination and boundary conditions, and numerical treatment

An integral quantity such as the simulated tumor outcome descriptor (or effective tumor burden) $V^*$ is desired, based on solution of Eq. (2), in order to compared with $V$ at times designated by the clinical assessments:

$$V^*(t) = \int_{\Omega_0} \phi_c \mathrm{d}\Omega \tag{7}$$

with $\Omega_0$ corresponding to $K$ in Eq. (1) (or geometrical volume of the entire mammary gland). In order to perform the integration of Eq. (2), an initial condition $\phi_{ci}$ is needed, corresponding to a conventional, small enough tumoral lesion or early-stage BC (nominally taken as 3 orders of magnitude smaller than $\Omega_0$):

$$V^*(t = t_i) = \phi_{ci} \cdot \Omega_0 \tag{8}$$

while for computations resulting in pCR a termination condition $\phi_{cs}$ is needed, nominally taken as 1 order of magnitude smaller than $\phi_{ci}$.

As $\Omega_0$ is wrapped up in the control surface $\partial\Omega_0$, a no-flux boundary condition is finally applied (in the said limit of early-stage BC):

$$\left.\frac{\partial \phi_c}{\partial \mathbf{x}}\right|_{\partial\Omega_0} = 0 \tag{9}$$

In the end, $\phi_c$ will evolve in space and time making $V^*$ inflate/deflate according to the above biological and biochemical descriptors and constraints.

As a diagnostic imaging sequence such as Fig. 1.**b**, produces a DICOM file format stack, image segmentation and 3D reconstruction for computational modeling purposes must be performed [12,24,25]. A discretized ROI is obtained as in Fig. 2, completed with the representation of the internal lesion. Then 3D tumor model ROIs are exported to a FEM software by means of STL file format, so that the above PDEs model can be applied and solved [21,26]. The use of a widely adopted, off-the-shelf FEM platform is purposeful as it ensures numerical robustness, traceability of the discretization and solver settings, and straightforward reproducibility of the results.

The computational domain was discretized using a prismatic mesh, generated to ensure adequate spatial resolution of gradients of $\phi$s while maintaining computational efficiency. Uniform element sizing was applied throughout the ROI, except a slight mesh refinement introduced in the vicinity of the initial lesion, where sharper gradients were expected. Grid independency was analyzed as reported in Table 1, so that Mesh level 2 was employed in each case, to optimize result accuracy and computational times on a Pentium Xeon®server (Windows®2019 Server OS [Microsoft, Redmont, WA, USA], Eightcore-32N at 2.4 GHz, 128 GB RAM).

## 3. Results

### 3.1. Patient cohort, regimen and virtual biomarkers details

A cohort of 15 Human Epidermal growth factor Receptor 2 positive (HER2+) BC patients was scrutinized by Di Modica et al. [27]. The treatment regimen included four cycles of EC chemotherapy branch (epirubicin plus cyclophosphamide) every 21 days, followed by twelve cycles of TH immunotherapy branch (taxol plus trastuzumab) every 7 days. Fecal samples were collected prior to the initiation of TH therapy. In brief, EC impairs replication and metabolism, with TH inhibiting division and signaling — both inducing tumor damage, mass reduction, and changes in transport, density, and biomechanical properties [28]. These clinical results were employed by De Bonis et al. [13] to validate the same model reported here in training and testing cohort subsets, to find the best $(r, \epsilon_{PD1}, \epsilon_{PD2})$ value set, as earlier alluded to. For such two-branch NAT study, a constraint was applied to ensure that the volume reduction induced by the EC branch accounted, on average, for 50% of the total volume decrease.

In the present paper, the following reference values that were uniformly assumed across the patient cohort: $D_c = 1 \cdot 10^{-12}$ m$^2$/s, $D_{d1} = D_{d2} = 1 \cdot 10^{-8}$ m$^2$/s, $r_0 = 1 \cdot 10^{-7}$ 1/s and $\epsilon_{PD02} = 5.0 \cdot 10^{-3}$ 1/s.

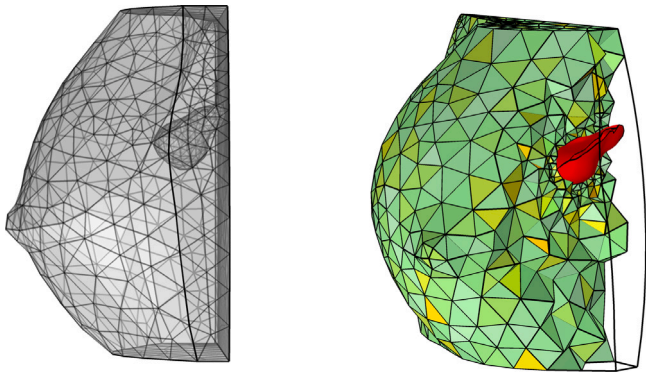

**Fig. 2.** Two views of the discretized control volume [12] corresponding to Fig. 1.**b**. As a volume inset, the tumoral lesion can be evidenced.

**Table 1**
Grid independence analysis, for Patient 9 presented later, showing the evolution of simulated lesion volume $V^*$ and the typical computational cost for successive mesh refinements.

| Mesh level | Elements | DOFs | Rel. change at $t = 0$ [%] | Rel. change at $t = \Delta t_s$ [%] | CPU time [h:mm:ss] |
|---|---|---|---|---|---|
| 1 | 7584 | 4425 | – | – | 0:39:25 |
| 2 | 13,518 | 7692 | 3.15 | 0.18 | 0:52:26 |
| 3 | 39,995 | 21,837 | 3.73 | 3.47 | 1:19:23 |
| 4 | 153,257 | 81,009 | 2.90 | 7.25 | 4:05:32 |

### 3.2. The continuum/discrete conundrum in quantitative oncology

Macroscopic lesion volume $V$ assessment depends on clinical evaluation of disruption in tissue density, vascularity continuity, or cell metabolism. Such evaluations lead to define the *cancer/healthy* quality of tissue, but this binary aspect defies the mechanistic formulation of Eq. (2), as $\phi_c(\mathbf{x}, t)$ is continuous in the ROI, instead. To illustrate this conundrum, two extremal scenarios are provided in Fig. 3, Left:

- Pure tumor diffusion, scenario A: starting from an initial cancer cells budget, $V^*$ is inflated due to the diffusive flux in the ROI, after some time $\Delta t$. No new cells are produced during this process, and the cells budget is conserved.
- Pure tumor production, scenario B: starting from the same initial cancer cells budget, $V^*$ is inflated due to the production flux in the ROI of incompressible biological material, but maybe to a lesser extent. Many new cells are produced during this process.

Cells budget in scenario A would remain the same, the volume of the lesion becoming larger than the initial one; while a growing budget would result in scenario B, but maybe contained in a smaller final

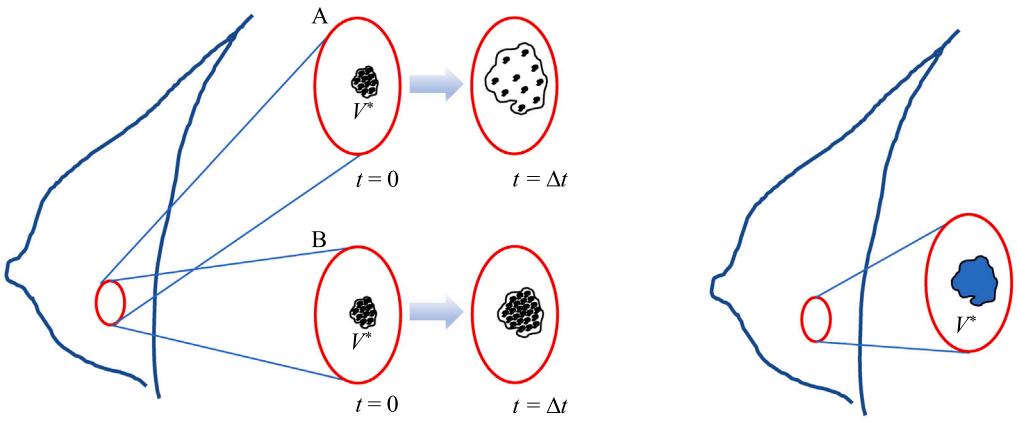


**Fig. 3. Left**: a rendering of a mammary gland's sagittal section, with a tumoral lesion highlighted. Close-ups are reported, at the beginning ($t = 0$) and at the end ($t = \Delta t$) of the observation, corresponding to extremal proliferation behaviors: scenario A – pure diffusion; scenario B – pure generation. Computed tumor metric $V^*$ is contoured by a black line. **Right**: a shaded area represents the *cancer tissue* label of the lesion, obtained by applying the threshold value at $\phi_c > T \cdot \phi_{ci}$, with threshold coefficient $T$ larger than 1 (assumed uniform across the cohort). Regions not meeting this criterion are classified as *healthy tissue*.

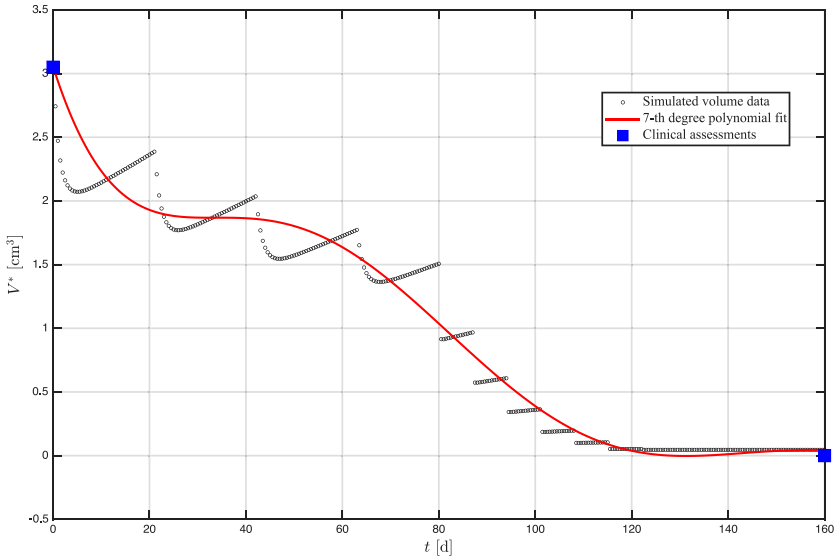


**Fig. 4.** Computational tumor volume reduction over time and related clinical assessment from diagnostic imaging (blue squares) for Patient 9 undergoing pCR. $\epsilon_{PD1} = 5.0 \cdot 10^{-5}$ 1/s is enforced in this case. Clinical assessments: $V(t = 0) = 3.05$ cm$^3$, $V(t = \Delta t_s) = 0$ cm$^3$. A polynomial averaging red curve is provided. (For interpretation of the references to color in this figure legend, the reader is referred to the web version of this article.)

volume than that of scenario A. It is evident that, for the diffusive-reactive process at hand, no clear address exists on how $\phi_c(\mathbf{x}, t)$ would contribute to the *cancer/healthy* tissue labeling.

A common alternative to the integral approach of Eq. (7), as shown first by Gatenby and Gawlinski [2], is the level-set or phase-field method, where a threshold value of $\phi_c$ (assumed uniform across the cohort at hand) is used to define a sharp interface between *cancer/healthy* tissues. In this way, an iso-surface can be extracted from a smooth $\phi_c$ distribution, as illustrated by Fig. 3. In this study, since imaging assessments were available only at $t = 0$ and $t = \Delta_s$, model validation relied upon macroscopic comparisons between $V$ and $V^*$, only, and Eq. (7) was enforced without further implementation. Likewise, a nominal ROI volume $\Omega_0$ of 1000 cm$^3$ was uniformly assumed across the patient cohort, which was a reasonable choice when dealing with early-stage disease.

### 3.3. Simulation of lesion volume for two validated sample patients

Fig. 4 is reported to show the typical lesion volume $V^*$ progress during a successful NAT sequence (Phase II in Fig. 1.**a**) for a patient undergoing pCR. The series of / series is evident, encompassing the entire observation time $\Delta t_s$ of both administered therapies. Another situation is depicted in Fig. 5 for a patient whose pCR was not achieved. In Fig. 4, perfect validation was achieved at the end of Phase II, while an absolute difference of only $2.42 \cdot 10^{-2}$ cm$^3$ was found in Fig. 5, again at the end of Phase II.

### 3.4. Impact of a different value of effective diffusion coefficient $D_c$

Fig. 6 is reported to show the effect of varying $D_c$ in the lesion volume $V^*$ progress for Patient 4, when using the two limiting values of the allowable $10^{-12}$–$10^{-13}$ m$^2$/s range [22]. It is seen that a modified value of $D_c$ would considerably perturb the solution, up to a more that 100% larger estimate at the end of the observation time $\Delta t_s$. In both such case, the same $(r, \epsilon_{PD1}, \epsilon_{PD2})$ virtual biomarkers value set was employed (as optimized for the reference diffusivity case), so that another set must be determined for validation, when allowing for a modified effective diffusivity.

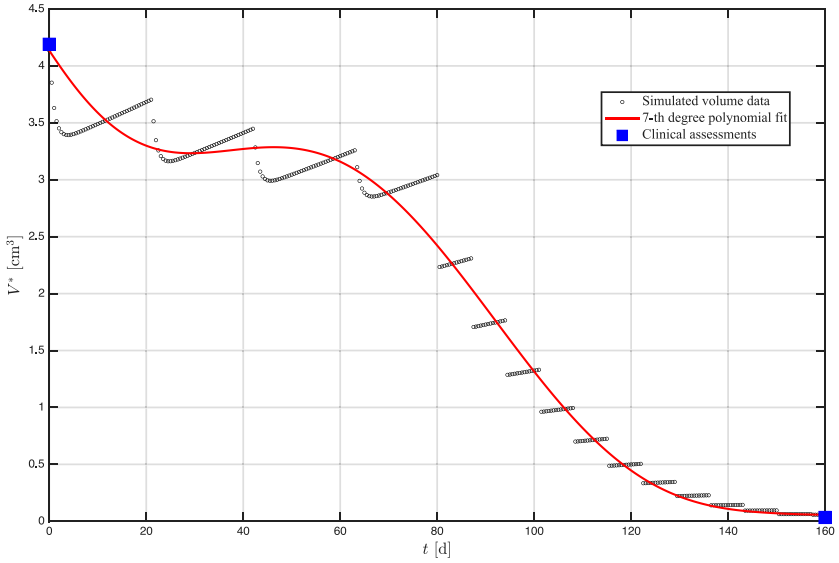


**Fig. 5.** Computational tumor volume reduction over time and related clinical assessment from diagnostic imaging (blue squares) for Patient 5, no pCR. $\epsilon_{\mathrm{PD1}} = 1.9 \cdot 10^{-5}$ 1/s is enforced in this case. Clinical assessments: $V(t = 0) = 4.19$ cm$^3$, $V(t = \Delta t_{\mathrm{s}}) = 3.35 \cdot 10^{-2}$ cm$^3$. A polynomial averaging red curve is provided. (For interpretation of the references to color in this figure legend, the reader is referred to the web version of this article.)

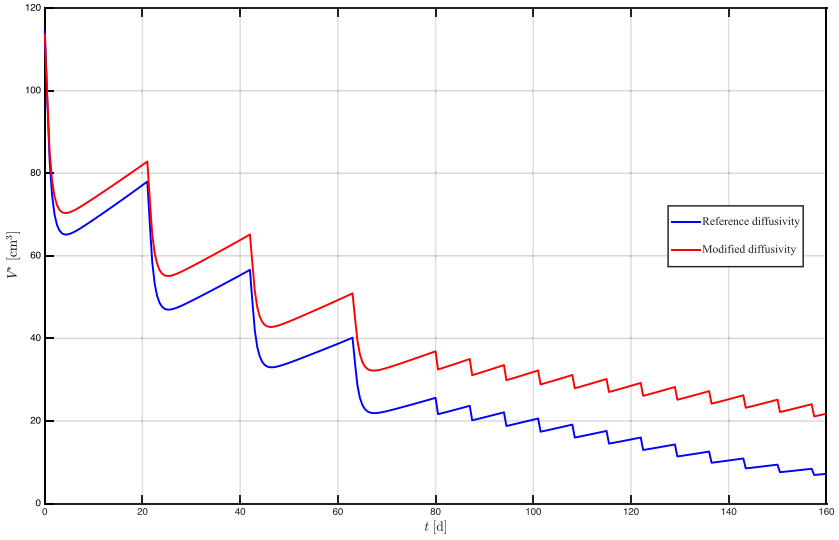


**Fig. 6.** Computational tumor volume reduction over time for Patient 4, no pCR, with two values of $D_{\mathrm{c}}$: reference $1 \cdot 10^{-12}$ and modified $1 \cdot 10^{-13}$ m$^2$/s. (For interpretation of the references to color in this figure legend, the reader is referred to the web version of this article.)

### 3.5. Optimizing neoadjuvant therapies by engineering metrics

It is evident that tumor proliferation and therapy effect follow a complex dynamic pattern. Recalling Eq. (7), we wish to minimize the residual lesion volume, before the surgical treatment, for a NAT composed by a sequence of 2 branches

$$\Delta V_{\mathrm{s}}^* = V^*(t = \Delta_{\mathrm{s}}) = \int_{\Omega_0} \left[\phi_{\mathrm{c}}(\mathbf{d}_1) + \phi_{\mathrm{c}}(\mathbf{d}_2)\right] \mathrm{d}\Omega \Big|_{t=\Delta t_{\mathrm{s}}} \tag{10}$$

by choosing a dosing schedule parameterized by discrete dose quantities $\mathbf{d}_{\mathrm{j}} = (d_1, \dots, d_{\mathrm{Nj}})$ given at fixed times and pulse durations, subject to the mass conservation constraint $\sum_{\mathrm{k}=1}^{\mathrm{Nj}} d_{\mathrm{k}} = M_{\mathrm{j}}$. Generally in many clinical settings, small dose deviations are common and acceptable due to rounding to vial sizes, body-surface-area approximations, or small practical variations: many cytotoxic regimens permit small deviations within their range without requiring re-prescription or dose-limiting toxicity calls. Therefore, here NAT is assumed to be subject to slight modifications (quantitative escalation or de-escalation) of certain pulses, to increase certain transient PD peaks.

In order to explore the complex transport phenomena setting at hand, let us then introduce a key reactive-diffusive metric by recalling Eq. (4), to compare such driving forces during Phase II (Fig. 1.**a**): a volume-averaged, instantaneous *Damköhler number* for a two-branch NAT can be cast as

$$\langle \mathrm{Da}_{r\epsilon} \rangle(t) = \frac{\text{volume-averaged reactive rate}}{\text{volume-averaged diffusive rate}} = \frac{L^2}{D_{\mathrm{c}} \Omega_0} \int_{\Omega_0} \left[ r \ln\left(\frac{K}{\phi_{\mathrm{c}}}\right) - \frac{\epsilon_{\mathrm{PD},1} \phi_{\mathrm{d},1}}{\phi_{\mathrm{c}}} - \frac{\epsilon_{\mathrm{PD},2} \phi_{\mathrm{d},2}}{\phi_{\mathrm{c}}} \right] \mathrm{d}\Omega \tag{11}$$

where $L$ is a fixed characteristic diffusion length in the ROI (such as $\Omega_0/\partial\Omega_0$), so to decouple kinetic sensitivity from morphological regression during treatment. In said early-stage BC assumption, $L = 5.8$ cm is assumed uniform across the scrutinized patient cohort.

As an example, considering Patient 4 (no pCR), four pronounced negative transients are observed corresponding to the EC branch 1

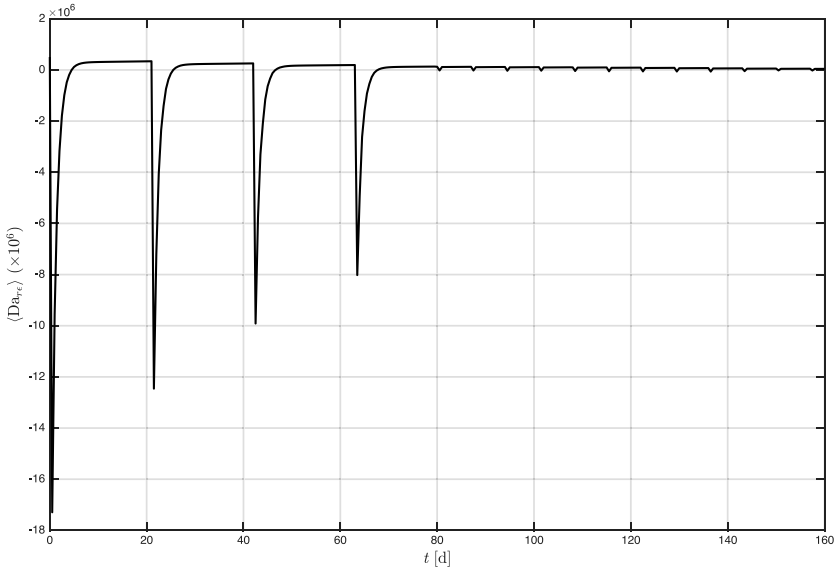


**Fig. 7.** Volume-averaged, instantaneous progress of Damköhler number $\langle \mathrm{Da}_{r\epsilon} \rangle$ for Patient 4, showing four pronounced transients corresponding to the four cycles of EC therapy branch with $\mathbf{d}_{10} = (1, 1, 1, 1)$. $\epsilon_{\mathrm{PD1}} = 7.0 \cdot 10^{-4}$ 1/s is enforced in this case.

in Fig. 7 when elevated drug concentrations, not yet attenuated by pharmacokinetic clearance, induce therapeutic effects with a temporal rate exceeding that of diffusive spatial equilibration ($\langle \mathrm{Da}_{r\epsilon} \rangle \ll -1$). Therefore, let us compare in Fig. 8 lesion volumes computed by different 2 scenarios for branch 1: a reference dosage $\mathbf{d}_{10} = (1, 1, 1, 1)$, and 2 modified dosages $\mathbf{d}_{1\nearrow} = (0.9, 0.95, 1.05, 1.1)$ or $\mathbf{d}_{1\searrow} = (1.1, 1.05, 0.95, 0.9)$, where arrows denote a linear quantitative escalation or de-escalation mode.

As the differences are not pronounced enough in Fig. 8, given the very slight change in dosage that was applied, let us introduce the following 3 descriptors to assess the relative merit of the given dosage schedule, as the normalized Therapeutic Performance index (TP), the Relative Improvement index between reference and mode k dosage (RI), and the residual lesion volume difference between reference and mode k dosage $\Delta V_{\mathrm{k}}^*$, as

$$\mathrm{TP} = \int_{\Omega_0} \left[ \phi_{\mathrm{c}}(t = 0) - \phi_{\mathrm{c}}(t = \Delta t_{\mathrm{s}}) \right] \mathrm{d}\Omega \tag{12}$$

$$\mathrm{RI}_{\mathrm{k}} = \frac{\mathrm{TP}_{\mathrm{k}} - \mathrm{TP}_0}{\mathrm{TP}_0} \times 100\% \tag{13}$$

$$\Delta V_{\mathrm{k}}^* = \int_{\Omega_0} \sum_{\mathrm{j}} \left[ \phi_{\mathrm{c}}(t = \Delta t_{\mathrm{s}})\big|_{\mathbf{d}_{\mathrm{j}0}} - \phi_{\mathrm{c}}(t = \Delta t_{\mathrm{s}})\big|_{\mathbf{d}_{\mathrm{jk}}} \right] \mathrm{d}\Omega \tag{14}$$

The TP index, considering a uniform exposure to NAT for all dosage schedules (i.e. conservative with respect to the total amount of administered drug), quantifies the efficiency of a therapy in converting the administered drug exposure into effective tumor reduction, while the RI index compares different treatment dosages with respect to the reference one, quantifying the percentage gain (or loss, if negative) in therapeutic performance of dosage mode k relative to a baseline or clinically standard schedule. Finally, $\Delta V_{\mathrm{k}}^*$ quantifies metrically for the dosage mode k the differential loss (or gain, if negative) of tumor volume with respect to the reference dosage.

As reported on Table 2, $\mathbf{d}_{1\searrow}$-type dosage schedule, would lead to better Therapeutic Performance for Patient 4: the dosage results in a residual lesion volume that is 0.33 cm$^3$ smaller than with the reference dosage. This result can be attributed to nonlinear pharmacodynamics in the intertwined tumor-drug PDE transport. It must be added that even if the final tumor volume appears to shrink only to an additional fraction of a cubic centimetre, such reductions are still clinically meaningful: in oncological prognosis, even minimal residual-disease improvements can significantly influence recurrence risk, surgical feasibility, and long-term survival. Therefore, what may seem a marginal numerical improvement in simulations can represent a substantial therapeutic benefit in real clinical practice. Finally, an improvement increment is obtained when yet another dosage modification is proposed for the same patient, namely an initially stronger dose with de-escalation $\mathbf{d}_{1\searrow\searrow} = (1.2, 1.1, 0.9, 0.8)$, favoring a final lesion volume 0.70 cm$^3$ smaller than the one obtained by the reference dosage.

**Table 2**
Summary metrics for sample Patients 4 and 11 [13]: Therapeutic Performance index (TP), Relative Improvement index (RI) and residual lesion volume difference ($\Delta V_{\mathrm{k}}^*$).

| Patient nr., dosage mode | TP index | $\mathrm{RI}_{\mathrm{k}}$ index | $\Delta V_{\mathrm{k}}^*$ [cm$^3$] |
|---|---|---|---|
| 4, $\mathbf{d}_{10}$ | 107.61 | – | 0 |
| 4, $\mathbf{d}_{1\searrow}$ | 107.95 | 0.31 | 0.33 |
| 4, $\mathbf{d}_{1\nearrow}$ | 107.35 | −0.24 | −0.26 |
| 4, $\mathbf{d}_{1\searrow\searrow}$ | 108.31 | 0.65 | 0.70 |
| 11, $\mathbf{d}_{10}$ | 8.4245 | – | 0 |
| 11, $\mathbf{d}_{1\searrow}$ | 8.4244 | −0.0059 | −0.00005 |
| 11, $\mathbf{d}_{1\nearrow}$ | 8.4242 | −0.0033 | −0.00028 |

$\langle \mathrm{Da}_{r\epsilon} \rangle$-driven dosage modulation examples shown here could be even better promoted if the tumor density could be set as dependent on drug exposure, improving drug penetration depth: in this way, later lower dosing will be diffusing more effectively. In other words, higher doses will be employed when tumor is relatively large and hard to penetrate, with lower doses when tumor has shrunk and easier to penetrate.

Examination of the $\langle \mathrm{Da}_{r\epsilon} \rangle$ and comparison of the outcomes with modified dosages $\mathbf{d}_{1\searrow}$ or $\mathbf{d}_{1\nearrow}$ is also reported for Patient 11 (pCR), with data reported in Fig. 9 and Table 2. In this case, dosage modification does not produce discernible changes in the final tumor volume.

This report highlights that the Damköhler number-based metric, by quantifying the imbalance between reactive and diffusive transport, can identify regimes in which clinically meaningful differential outcomes may be achieved through targeted dosage modification only when transient reaction intensities exceed a reference threshold, e.g. $\left|\langle \mathrm{Da}_{r\epsilon} \rangle\right| \gtrsim 10^6$ for Patient 4 in Fig. 7. This limiting value should be interpreted as a model- and cohort-specific indicator emerging from the proposed proof of concept, rather than as a universal constant. Accordingly, $\langle \mathrm{Da}_{r\epsilon} \rangle$ should be examined separately for each patient, and dose adaptation

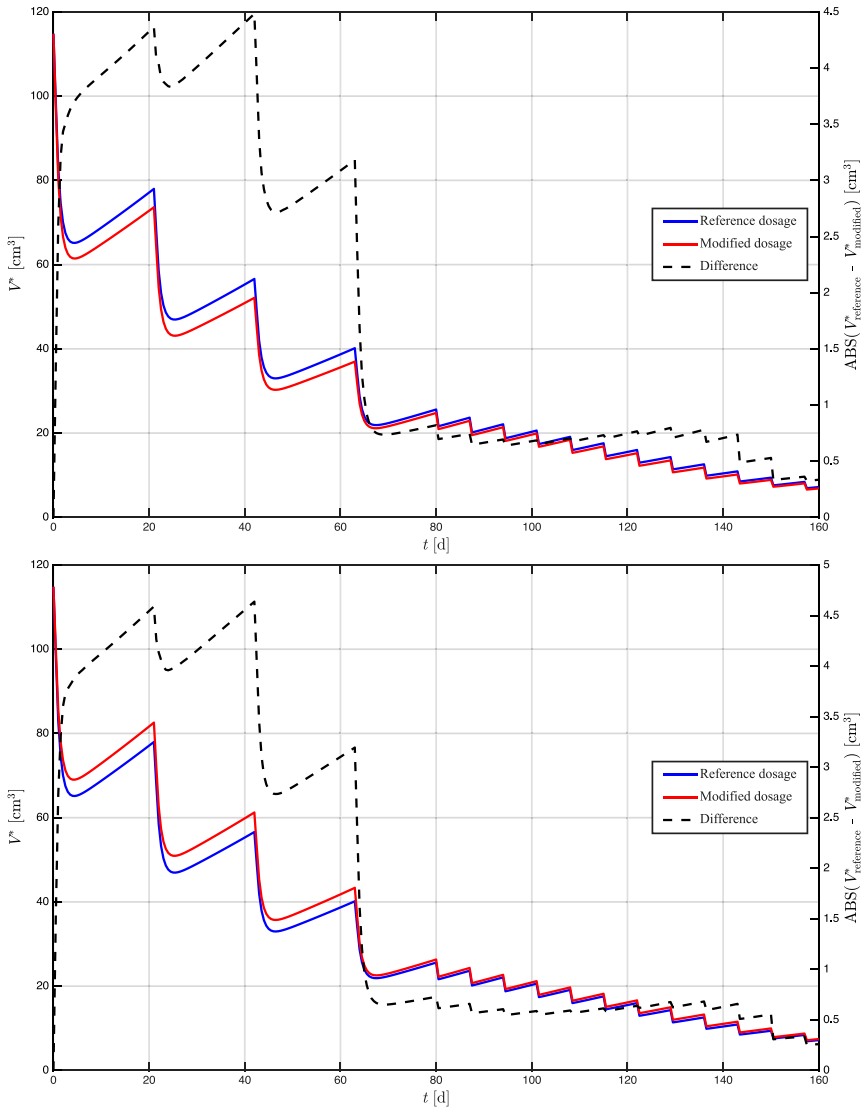


**Fig. 8.** Comparison of different dosage schedules as residual lesion volume $V^*$ and difference progress for Patient 4. **Top**: $\mathbf{d}_{10}$ (reference) vs. $\mathbf{d}_{1\nearrow}$ (escalation modified). **Bottom**: $\mathbf{d}_{10}$ (reference) vs. and $\mathbf{d}_{1\searrow}$ (de-escalation modified). The blue/red curve are read on the left axis, while the dashed black curve corresponds to the right axis, as indicated by the respective axis labels. Clinical assessments: $V(t=0) = 113$ cm$^3$, $V(t=\Delta t_s) = 0.100$ cm$^3$. (For interpretation of the references to color in this figure legend, the reader is referred to the web version of this article.)

for therapeutic benefit should be considered only when the governing PDE ensemble exhibits sufficient reactive dominance.

Lastly, a further dosage modification was explored, again for Patient 11, consisting in administering $\mathbf{d}_{1\searrow} + \mathbf{d}_{2\searrow}$, with

$$\mathbf{d}_{1\searrow} = (1.1, 1.05, 0.95, 0.9), \qquad \mathbf{d}_{2\searrow} = (1.1, 1.1, 1\times 8, 0.9, 0.9)$$

i.e. considering the second NAT branch, also. In this case, achievement of pCR is anticipated by approximately 15 days (Fig. 10), resulting in a shorter interval during which tumor burden remains clinically relevant. While this time reduction is not intended to directly predict changes in recurrence risk or long-term survival, it represents a measurable improvement in treatment efficiency. From a systems-level perspective, earlier tumor eradication may reduce cumulative exposure to cytotoxic agents and shorten the duration of disease-related physiological stress, which are factors commonly associated with treatment tolerability and patient-reported outcomes. Accordingly, the present result should be interpreted as a quantitative indication of potential benefit in treatment course optimization, rather than as a direct surrogate for long-term clinical endpoints.

Finally, it is worth emphasizing that an interesting application of the proposed framework is its integration into an artificial intelligence (AI) pipeline to mitigate a major bottleneck in predictive oncology, namely the scarcity, heterogeneity, and longitudinal inconsistency of clinical datasets. By quantitatively modeling BC therapy response and validating simulations against retrospective cohorts, the framework would enable the generation of virtual patients whose tumor volume progress is constrained by mechanistic principles rather than arbitrary or statistical interpolation. Systematic exploration of the model parameter space – including treatment schedules, genetic scores, and new biomarkers such as the ones purported so far – can then yield large, clinically realistic in-silico response datasets for entire BC subtypes and drug libraries. In turn, these virtual cohorts could provide scalable, ethically unconstrained training data for AI models, supporting the development and benchmarking of our model while preserving fidelity to tumor dynamics and reducing dependence on slow and costly patient recruitment.

## Conclusions

This predictive oncology project, for a cohort of HER2+ breast cancer patients, was elaborated by considering a common sequence of

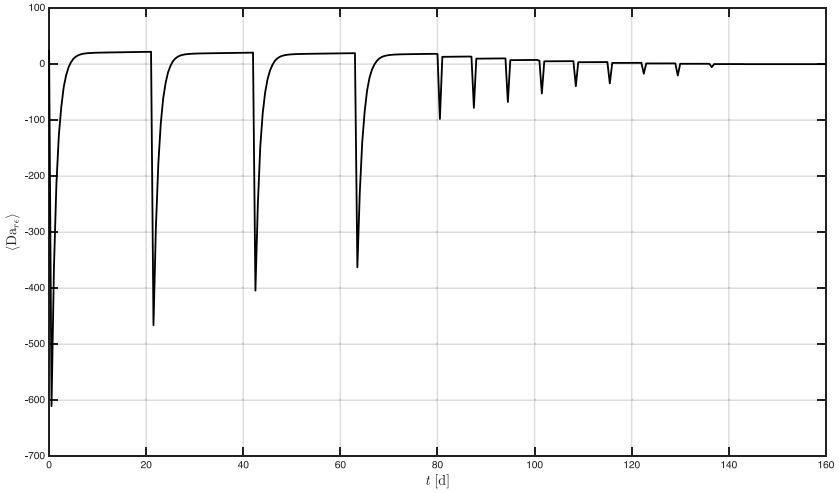


**Fig. 9.** Volume-averaged, instantaneous progress of Damköhler number $\langle \mathrm{Da}_{rc} \rangle$ for Patient 11 [13], showing again four pronounced transients corresponding to the four cycles of EC therapy branch, with $\mathbf{d}_{10} = (1, 1, 1, 1)$, but with much weaker transients when compared to those in Fig. 7. $\epsilon_{\mathrm{PD1}} = 4.2 \cdot 10^{-5}$ 1/s is enforced in this case.

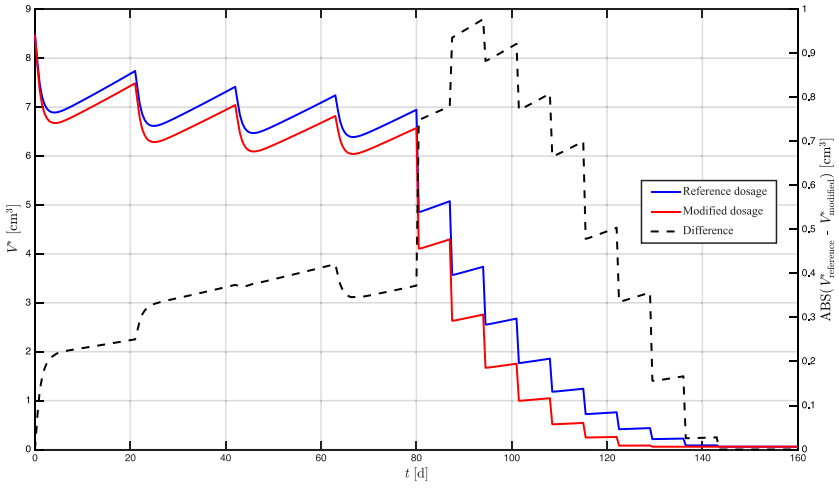


**Fig. 10.** Volume-averaged, instantaneous progress of Damköhler number $\langle \mathrm{Da}_{rc} \rangle$ for Patient 11 [13], showing again four pronounced transients corresponding to the four cycles of EC therapy branch, with $\mathbf{d}_{10} = (1, 1, 1, 1)$, but with much weaker values when compared to Fig. 7. $\epsilon_{\mathrm{PD1}} = 4.2 \cdot 10^{-5}$ 1/s is enforced in this case. (For interpretation of the references to color in this figure legend, the reader is referred to the web version of this article.)

two different neoadjuvant therapies, suggesting possible ways to implement clinical optimization. We showed that controlled per-pulse dose reallocations of up to $\pm 10\%$, generally compatible with current clinical practice, are mathematically straightforward and revealing of personalized therapy improvement. Within the proposed CFD-PDE framework, even such modest redistributions can leverage the nonlinearities of the PDEs ensemble (mainly the PK/PD interactions) simulating tumor dynamics, as captured by specially designed metrics: a Free Proliferation number (FP), a Therapeutic Performance index (TP), a Relative Improvement index (RI), and an oncological Damköhler number $\langle \mathrm{Da}_{rc} \rangle$. The approach enables a transition from cohort-level prediction toward personalized treatment guidance: in particular, the $\langle \mathrm{Da}_{rc} \rangle$ number identifies treatment phases in which local kinetics are most sensitive to additional drug input, enabling targeted optimization rather than uniform administrations. As a result, selected schedules yield reduced residual tumor volume or shortened time to complete response — without increasing overall exposure to drugs. This study has therefore demonstrated its feasibility towards motivate future clinical validations.

While the present framework captures treatment response at the macroscopic tumor level, its modular structure could allow straightforward extensions toward personalization by incorporating variability in drug clearance due to individual hepatic and renal functions, without altering the core governing equations. In this perspective, practical implementations need to integrate toxicity constraints, therapeutic drug monitoring, and schedule regularization (even by more formal optimization algorithms), ensuring that optimized regimens remain both personalized and feasible within standard-of-care protocols. The absence of intermediate imaging time points – reflecting standard clinical practice and thus constituting a data-availability constraint rather than a modeling assumption – motivates the present integral formulation, while intermediate time points would advance the present modeling approach toward level-set implementations capable of resolving smooth cancer/healthy tissue interfaces, closer to virtual twins deployment. The use of a widely adopted, off-the-shelf FEM platform is already playing a strategical role to that extent, ensuring numerical feasibility. Finally, the presented approach could provide the core engine for generating realistic synthetic data to feed generative AI models, to accelerate the clinical adoption of this computational framework.

Ultimately, this work suggests a closed-loop strategy enforcing computational prognosis – model prediction, clinician assessment, patient monitoring, and periodic model updating – allowing therapy schedules to be refined in a data-informed and patient-specific manner.

## Nomenclature

| | |
|---|---|
| $D$ | Diffusion coefficient, $m^2/s$ |
| $\mathbf{D}$ | Diffusion coefficient tensor, $m^2/s$ |
| $\mathbf{d}$ | Normalized dose fraction, dimensionless |
| $K$ | Carrying capacity of the biological matrix, dimensionless |
| $M$ | Total administered therapy mass, kg |
| $\dot{m}$ | Administered mass flow rate, determined on personalized basis, $mol/m^3$ s |
| $N$ | Number of doses |
| $r_c$ | Biological conversion rate, 1/s |
| $R$ | Source terms in Eqs. (2), (3), 1/s |
| $t$ | Time, d |
| $V^*$ | Computed lesion volume, $cm^3$ |
| $V$ | Measured lesion volume, $cm^3$ |
| $\mathbf{x}$ | Coordinate vector, cm |
| *Greek* | |
| $\Delta t_s$ | NAT duration (before surgical treatment if no pCR), d |
| $\Delta V_s$ | Residual lesion volume to remove surgically after NAT, $cm^3$ |
| $\epsilon_{PD}$ | Aggregated drug efficiency (effect of drug on body), 1/s |
| $\epsilon_{PK}$ | Drug clearance (effect of body on drug), 1/s |
| $\partial\Omega$ | External surface, $m^2$ |
| $\phi_c$ | Normalized cancer cell density or volume, dimensionless |
| $\phi_d$ | Drug concentration, $mol/m^3$ |
| $\Omega$ | Computational volume, $cm^3$ |
| *Subscripts* | |
| 0 | Nominal, reference |
| c | Cancer |
| d | Drug |
| e | Interface with the environment |
| i | Initial |
| j | Drug counter |
| k | Dose counter |
| s | After NAT |

## Abbreviations

| | |
|---|---|
| BC | Breast cancer |
| | Effect of the interaction between tumor growth rate and therapeutic dynamics |
| CFD | Computational Fluid Dynamics |
| DI | Gut Microbiota Diversity Index |
| DICOM | Digital Imaging and Communications in Medicine file format |
| FEM | Finite Element Method |
| FP | Dimensionless Free Proliferation number |
| | Effect of the interaction between growth rate and drug clearance |
| NAT | Neoadjuvant therapy |
| pCR | Pathological Complete Response |
| PD | Pharmacodynamics |
| PDE | Partial Differential Equation |
| PK | Pharmacokinetics |
| PDE | Partial Differential Equation |
| RI | Relative Improvement index |
| ROI | Region Of Interest |
| STL | STereo Lithographic file format |
| TP | Normalized Therapeutic Performance index |

## CRediT authorship contribution statement

**Gianpaolo Ruocco:** Writing – review & editing, Writing – original draft, Visualization, Validation, Supervision, Software, Resources, Methodology, Investigation, Formal analysis, Data curation, Conceptualization.

## Declaration of competing interest

The authors declare that they have no known competing financial interests or personal relationships that could have appeared to influence the work reported in this paper.

## References


[1] World Health Organisation, Breast cancer, 2026, Available Online: (https://www.who.int/news-room/fact-sheets/detail/breast-cancer), (Accessed 26 February 2026).

[2] R.A. Gatenby, E.T. Gawlinski, A reaction-diffusion model of cancer invasion, Cancer Res. 56 (24) (1996) 5745–5753, http://dx.doi.org/10.1158/0008-5472.CAN-96-5745.

[3] A.R. Anderson, M.A.J. Chaplain, E.L. Newman, R.J. Steele, A.M. Thompson, Mathematical modelling of tumour invasion and metastasis, Comput. Math. Methods Med. 2 (2) (2000) 129–154, http://dx.doi.org/10.1080/10273660008833042.

[4] G. Stamatakos, D. Dionysiou, N. Graf, N. Sofra, C. Desmedt, A. Hoppe, D. Kolokotroni, A. Dimitrakopoulou, The 'Oncosimulator': A multilevel, clinically oriented simulation system of tumor growth and organism response to therapeutic schemes. Towards the clinical exploitation of in silico oncology, IEEE Eng. Med. Biol. Mag. 26 (5) (2007) 45–53, http://dx.doi.org/10.1109/MEMB.2007.4338475.

[5] V. Cristini, J. Lowengrub, Multiscale Modeling of Cancer: An Integrated Experimental and Mathematical Modeling Approach, Cambridge University Press, United Kingdom, 2010, pp. 24–30, http://dx.doi.org/10.1017/CBO9780511781452.

[6] J.A. Weis, M.I. Miga, L.R. Arlinghaus, X. Li, A.B. Chakravarthy, V. Abramson, J. Farley, T.E. Yankeelov, A mechanically coupled reaction–diffusion model for predicting the response of breast tumors to neoadjuvant chemotherapy, Phys. Med. Biol. 58 (17) (2013) 5851–5866, http://dx.doi.org/10.1088/0031-9155/58/17/5851.

[7] N. Ghaffari Laleh, C.M.L. Loeffler, J. Grajek, K. Staňková, A.T. Pearson, H.S. Muti, C. Trautwein, H. Enderling, J. Poleszczuk, J.N. Kather, Classical mathematical models for prediction of response to chemotherapy and immunotherapy, PLoS Comput. Biol. 18 (2) (2022) e1009822, http://dx.doi.org/10.1371/journal.pcbi.1009822.

[8] C. Wu, E.A. Lima, C.E. Stowers, Z. Xu, C. Yam, J.B. Son, T.E. Yankeelov, MRI-based digital twins to improve treatment response of breast cancer by optimizing neoadjuvant chemotherapy regimens, Npj Digit. Med. 8 (1) (2025) 195, http://dx.doi.org/10.1038/s41746-025-00000-0.

[9] P. Caccavale, M.V. De Bonis, G. Marino, G. Ruocco, Mass transfer modeling of solid tumor growth for therapy evaluation and prognosis, Int. Commun. Heat Mass Transfer 117 (2020) 104781, http://dx.doi.org/10.1016/j.icheatmasstransfer.2020.104781.

[10] G. Marino, M.V. De Bonis, L. Lagonigro, G. La Torre, A. Prudente, A. Sgambato, G. Ruocco, Towards a decisional support system in breast cancer surgery based on mass transfer modeling, Int. Commun. Heat Mass Transfer 129 (2021) 105733, http://dx.doi.org/10.1016/j.icheatmasstransfer.2021.105733.

[11] F. Schettini, M.V.D. Bonis, C. Strina, M. Milani, N. Ziglioli, S. Aguggini, I. Ciliberto, C. Azzini, G. Barbieri, V. Cervoni, M.R. Cappelletti, G. Ferrero, M. Ungari, M. Locci, I. Paris, G. Scambia, G. Ruocco, D. Generali, Computational reactive–diffusive modeling for stratification and prognosis determination of patients with breast cancer receiving Olaparib, Sci. Rep. 13 (2023) 11951, http://dx.doi.org/10.1038/s41598-023-38760-z.

[12] G. Marino, M.V. De Bonis, M. Mecca, M. Sichetti, A. Cammarota, M. Botte, G. Dinardo, M.I. Lancellotti, A. Villonio, A. Prudente, A. Thodas, E. Zifarone, F. Sanseverino, P. Modano, F. Schettini, A. Rocca, D. Generali, G. Ruocco, Virtual biomarkers and simplified metrics in the modeling of breast cancer neoadjuvant therapy: A proof-of-concept case study based on diagnostic imaging, Med. Sci. 13 (4) (2025) 242, http://dx.doi.org/10.3390/medsci13040242.

[13] M.V. De Bonis, T. Triulzi, M. Di Modica, F. Corsi, M. Francesconi, G. Marino, F. Schettini, E. Tagliabue, G. Ruocco, D. Generali, Computational modeling of lesion dynamics in HER2+ breast cancer: integrating gut microbiota diversity into therapy response prediction, Sci. Rep. (2026) submitted for publication.

[14] G.M. Thurber, Distribution and Metabolism of Antibodies and Other Macromolecules in Tumor Tissue (Ph.D. thesis), Massachusetts Institute of Technology, Cambridge, MA, 2008, URL https://dspace.mit.edu/handle/1721.1/45472.

[15] M. Petretta, G. Storto, T. Pellegrino, D. Bonaduce, A. Cuocolo, Quantitative assessment of myocardial blood flow with SPECT, Prog. Cardiovasc. Dis. 57 (6) (2015) 607–614, http://dx.doi.org/10.1016/j.pcad.2014.12.007.

[16] J.W. Baish, T. Stylianopoulos, R.M. Lanning, W.S. Kamoun, D. Fukumura, L.L. Munn, R.K. Jain, Scaling rules for diffusive drug delivery in tumor and normal tissues, Proc. Natl. Acad. Sci. 108 (5) (2011) 1799–1803, http://dx.doi.org/10.1073/pnas.1018154108.

[17] B. Erdogan, D.J. Webb, Cancer-associated fibroblasts modulate growth factor signaling and extracellular matrix remodeling to regulate tumor metastasis, Biochem. Soc. Trans. 45 (1) (2017) 229–236, http://dx.doi.org/10.1042/BST20160387.

[18] J.A. Weis, M.I. Miga, T.E. Yankeelov, Three-dimensional image-based mechanical modeling for predicting the response of breast cancer to neoadjuvant therapy, Comput. Methods Appl. Mech. Engrg. 314 (2017) 494–512, http://dx.doi.org/10.1016/j.cma.2016.08.020.

[19] M. Ptashnyk, C. Venkataraman, Multiscale modelling, analysis and simulation of cancer invasion mediated by bound and soluble enzymes, Bull. Math. Biol. 87 (11) (2025) 155, http://dx.doi.org/10.1007/s11538-025-01345-6.

[20] S.M. Wise, J.S. Lowengrub, H.B. Frieboes, V. Cristini, Three-dimensional multispecies nonlinear tumor growth—I: model and numerical method, J. Theoret. Biol. 253 (3) (2008) 524–543, http://dx.doi.org/10.1016/j.jtbi.2008.03.027.

[21] G. Ruocco, Introduction to Transport Phenomena Modeling: A Multiphysics, General Equation-Based Approach, Springer, 2019, http://dx.doi.org/10.1007/978-3-319-66822-2.

[22] N.M. Mirzaei, Z. Tatarova, W. Hao, N. Changizi, A. Asadpoure, I.K. Zervantonakis, Y. Hu, Y.H. Chang, L. Shahriyari, A PDE model of breast tumor progression in MMTV-PyMT mice, J. Pers. Med. 12 (5) (2022) 807, http://dx.doi.org/10.3390/jpm12050807.

[23] A. Rahman, S. Ghosh, Modeling of drug diffusion in a solid tumor leading to tumor cell death, Phys. Rev. E 98 (6) (2018) 062408, http://dx.doi.org/10.1103/PhysRevE.98.062408.

[24] 3D Slicer Community, 3D Slicer v.4.1, 2020, Software documentation, Available At https://www.slicer.org.

[25] R. Kikinis, S.D. Pieper, K.G. Vosburgh, 3D Slicer: A platform for subject-specific image analysis, visualization, and clinical support, in: Intraoperative Imaging and Image-Guided Therapy, Springer, 2013, pp. 277–289.

[26] COMSOL AB, COMSOL multiphysics v.5.6, 2020, Software documentation.

[27] M. Di Modica, G. Gargari, V. Regondi, A. Bonizzi, S. Arioli, B. Belmonte, A.D. Cecco, G. Bernasconi, S. Fiore, L. Minuzzo, S. Rossi, L. Caligola, L. Tognini, P. Sfondrini, A. Bruno, L.A. Di Martino, C. Mauri, C. Tramutola, F. Visioli, G. Motta, F. Marchesi, N. Pugno, E. Reggiani, G. Grandi, E. Tagliabue, Gut microbiota condition the therapeutic efficacy of trastuzumab in HER2-positive breast cancer, Cancer Res. 81 (8) (2021) 2195–2206, http://dx.doi.org/10.1158/0008-5472.CAN-20-1659.

[28] A. Schneeweiss, V. Möbus, H. Tesch, C. Hanusch, C. Denkert, K. Lübbe, J. Huober, P. Klare, S. Kümmel, M. Untch, K. Kast, C. Jackisch, J. Thomalla, B. Ingold-Heppner, J.-U. Blohmer, M. Rezai, M. Frank, K. Engels, K. Rhiem, P.A. Fasching, V. Nekljudova, G. von Minckwitz, S. Loibl, Intense dose-dense epirubicin, paclitaxel, and cyclophosphamide (iddEPC) in high-risk early breast cancer, Breast Cancer Res. Treat. 178 (3) (2019) 627–636, http://dx.doi.org/10.1007/s10549-019-05415-6.